Submitted for Publication in Radio Science, June 1995

An electrothermodynamic model with distributed properties for effective perrnittivities of sea ice

S. V. Nghiem and R. Kwok
Jet Propulsion Laboratory
California Institute of Technology
Pasadena, California

J. A. Kong and R. T. Shin
Department of Electrical Engineering and Computer Science
and Research Laboratory of Electronics
Massachusetts Institute of Technology
Cambridge, Massachusetts

S. A. Arcone and A. J. Gow
U.S. Army Cold Regions Research and Engineering Laboratory
Hanover, New Hampshire

Mail: JPL, MS 300-235, 4800 Oak Grove Dr., Pasadena, CA 91109

An electrothermodynamic model with distributed properties for effective permittivities of sea ice

S. V. Nghiem and R. Kwok

Jet Propulsion Laboratory, California in.qtitui e of Technology, Pasadena

J. A. Kong and R. T. Shin

Department of Electrical Engineering and Computer Science

and Research Laboratory of -Electronics

Massachusetts Institute of Technology, Cambridge

S. A. Arcone and A. J. Gow

U.S. Army Cold Regions Research and Engineering Laboratory

Hanover, New Hampshire

This paper presents a model to calculate the temperature dependence of effective permit tivit ies for a 1 ıeterogeneous anisotropic medium containing multiphase scatterers. With the strong permittivity fluctuation approach, the model is developed to account for the electrodynamic scattering effect together with the quasi-static characteristics of multiple species and subspecies of inhomogeneities with distributed orientations, sizes, and shapes. Duc to a preferential direction in the orientation distribution, the medium is effectively

anisotropic. The size distribution is described with a probability density function in terms of normalized volumetric sizes. Scatterer shapes are nonuniform and have a genera] ellipsoidal form characterized by arbitrary axial ratios of correlation lengths which arc related to physical geometries of the scatterers. In this formulation, sea ice consisting of solid ice, liquid brine, and gaseous inclusions is modeled to derive anisotropic effective permittivities with thermodynamic phase redistribution and structural metamorphism.. Theoretical results arc in good agreement with experimental data at 4.8 GHz for saline ice undergoing warming and cooling cycles. A competitive effect between the increase of liquid brine and the rounding of ellipsoidal scatterers at increasing temperatures explains the trend observed in measured data. Sensitivities of effective permittivities to structural and physical parameters characterizing sea ice arc also studied.

1. INTRODUCTION

Most natural media arc heterogeneous mixtures of materials with different phases, orientations, sizes, and shapes. Physical and struct ural characteristics of medium const it uents are usual] y interdependent and influenced by environment al conditions such as ambient temperature, solar radiation, moisture and precipitation. The composite media can be characterized by effective perrnittivities, w] ich determine elect romagnet ic wave propagation, at tenuation, scattering, and emission. These processes are essential to the

interpretation of remote sensing data of geophysical media. Effective permittivities themselves, however, also often demonstrates complex environmental dependencies such as thermal variations. This paper presents a permittivity model to explain these effects and illustrate the results with an application to sea ice.

Permittivities of mixtures have long been a subject of extensive study. Many dielectric mixing formulas have been derived for multiphase inhomogeneities with spherical, spheroidal, and ellipsoidal shapes. Together with a summary of these formulas, Tinga et al. [1975'] reported a formula for confocal ellipsoidal shell inclusions and compared calculated results with measured data for wet wood. In modeling of heterogeneous earth, Wait [1983] indicated that the particle shape is important to the effective electrical properties. A more complete account of electrical properties of the earth has been documented [*Wait,* 1989], including a model of coated particles for disseminated sulphide mineralization. With applications to snow and sea ice, Sihvola and Kong [*1988*] obtained a general mixing formula under the quasi-static condition for multiphase mixtures of scattering ellipsoids.

In addition to the quasi-static term, a scattering term appears in the effective permittivity expression derived from the strong permittivity fluctuation theory [*Tsang and Kong, 1981a].* In this approach, the quasi-static absorption loss and the dispersive scattering loss are both considered. The theory was applied to vegetation [*Tsang and Kong, 1981 b], snow* [*Tsang et al., 1982],* and sea ice [*Stogryn, 1987*]. This approach has been extended to model a random medium containing uniform ellipsoids with orientation distributions [*Nghiem et* al., *1993*] and an isotropic heterogeneous medium containing multiple species of uniform-size scatterers [*Nghiem et al., 1995b*].

In this paper, a model is developed to account for the complexity of multiphase

mixtures with multiple species and subspecies of scat terers characterized by orientation, size, and shapes distributions. With the strong fluctuation approach, derived effective permittivities will include scattering effects. The orientation distribution has a preferential alignment direction rendering the medium effectively anisotropic. The size distribution is described in terms of number density or fractional volume as a function of normalized volumetric size. The shape distribution affects electromagnetic properties of the mixture in a nonlinear manner. To depict various shapes of scatterers in a species, scatterers with a similar shape arc classified into a group treated as a subspecies.

The theory is used to obtain anisotropic effective permittivities of multiphase congelation sea ice with a columnar structure, In this formulation, physical and structural characteristics of the medium can be modeled more realistically. Moreover, the model allows physical and morphological variations in medium properties that are interrelated and subordinated to physical processes such as constituent phase redistribution and structural metamorphism under thermal effects. Calculated results arc compared with experimental data at 4.8 GHz for multiphase saline ice undergoing warming and cooling cycles.

2. MODEL FOR EFFECTIVE PERMITTIVITIES

In this section, the strong permittivity fluctuation approach is used to formulate and derive effective permit t ivities of an anisotropic medium cent aining scatterers with different phases, permittivities, and distributed structural properties. The effective permittivities arc obt ained by combining the method for an inhomogeneous ani sot ropic medium [*Nghiem et al., 1993*] with the method for a multi-species mixture [*Nghiem et al., 1995b*].

2.1. *Formulation for a Distributed Heterogeneous Medium*

The effective permittivity tensor of the medium consists of a quasi-static part and a scattering part corresponding to the first and second terms, respectively, in the following expression [*Tsang and Kong, 1981a]*

$$\bar{\bar{\epsilon}}_{eff} = \bar{\bar{\epsilon}}_g + \epsilon_0 \left[\bar{\bar{I}} - \bar{\bar{\xi}}_{eff} \cdot \langle \bar{\bar{S}} \rangle \right]^{-1} \cdot \bar{\bar{\xi}}_{eff} \tag{1}$$

where $\bar{\bar{I}}$ is the unit dyad. In (l), $\bar{\bar{\epsilon}}_g$ is the auxiliary permit, ttivity tensor, $\bar{\bar{S}}$ is the dyadic coefficient of the Dirac delta part in the dyadic Green's function of an anisotropic medium, and $\bar{\bar{\xi}}_{eff}$ is the, effective dyadic scatterer. Before deriving these quantities, wc need to describe the medium and define characterizing paramcters.

Figure 1 illustrates the modeling of a multiphase medium with multiple species and subspecies of scatterers such as sea, ice. First, define a species as a set of scatterers with tile same permittivity. In (1), $\bar{\bar{\epsilon}}_g$ and $\bar{\bar{S}}$ arc solved iteratively from a set of nonlinear coupled equations; these quantities depend on ratios of correlation lengths, i.e., scatterer shapes [*Nghiem et al., 1995 b*]. Thus, it is necessary to classify scatterers in each species into groups considered as subspecies; each contains scatterers of similar shape. In this context, a subspecies is a set of scatterers with the same permittivity *and* the same shape. The shapes have a general ellipsoidal form with arbitrary axial ratios including spheroids and spheres as special cases. While $\bar{\bar{\epsilon}}_g$ depends only on correlation length ratios, the scattering part in (1) dots depend on the scatterer size. Size validations of scatterers in a species are accounted for with an integration over the scatterer size distribution in the calculation of the scattering part.

Let ϵ_b be the permittivity of a background medium hosting a total number of N

scattering subspecies. Permittivity ϵ_{is} is for subspecies i occupying a fractional volume f_{is} in the mixture, The total fractional volume of all scatterers is $\sum_{i=1}^{N} f_{is} = 1 - f_b$ where f_b is the fractional volume of the background. Note that a single subscript i is used to denote subspecies in all species (this simplifies the arrangement of subspecies and species into a single array) and that ϵ_{is} has the same value for scatterers in the same species.

The effective dyadic scatterer, $\bar{\bar{\xi}}_{eff}$, of the heterogeneous anisotropic medium is given by the following expression [*Tsang and Kong, 1991a; Nghiem et al., 1993, 1995b*]

$$[\bar{\bar{\xi}}_{eff}]_{jm} = \sum_{i=1}^{N} \int_{v_i(species)} dv \int_0^{2\pi} d\gamma \int_0^{\pi} d\beta \int_0^{2\pi} d\alpha \; p_i(\alpha,\beta,\gamma)$$
$$\sum_{k,l}^{x,y,z} \Gamma^{(0)}_{i\xi jklm} \left\{ k_0^2 \int_{-\infty}^{\infty} d\bar{k}' \; [\bar{\bar{G}}_g(\bar{k}')]_{kl} \Phi_{i\xi}(\bar{k}') + [\bar{\bar{S}}_i]_{kl} \right\} \Bigg|_{v,\alpha,\beta,\gamma} \tag{2}$$

which is valid under the condition $\left|[\bar{\bar{\xi}}_{eff}(\bar{k})]_{jm}\right| << 1$. Normalized volumetric size v is defined as the volume of a scatterer in a species under consideration divide by the volume of the smallest scatterer of the same permittivity *regardless of shape*. By this definition, the minimum value of v is 1. The integration over dv accounts for the size distribution in the size range $v_i(species)$ of scatterers in a species. The probability density function of orientation $p_i(\alpha,\beta,\gamma)$ is described in terms of Eulerian orientation angles α, β, and γ, which relate the local coordinates (x', y', z') to the global system (x, y, z) as shown in Figure 2. The tensor $\bar{\bar{G}}_g$ is the anisotropic dyadic Green's function [*Nghiem et* al., *1990*]. For the ellipsoidal form of scatterers used in this paper, the Fourier transform $\Phi_{i\xi}$ of the normalized local correlation function is

$$\Phi_{i\xi}(\bar{k}') = \frac{\ell_{ix'}\ell_{iy'}\ell_{iz'}}{\pi^2(1 + k_x'^2\ell_{ix'}^2 + k_y'^2\ell_{iy'}^2 + k_z'^2\ell_{iz'}^2)^2} \tag{3}$$

in the local coordinates of the scatterer. The local correlation lengths $\ell_{ix'}$, $\ell_{iy'}$, and $\ell_{iz'}$ depend on the scatterer size and shape. The local variance $\Gamma^{(0)}_{i\xi jklm}$ of scatterer fluctuations

of subspecies i is defined as [*Nghiem et al., 1995b*]

$$\Gamma^{(0)}_{ijklm}(\bar{r}') = f_{is}(v) f_b \left(\xi_{ijk} - \xi_{bjk}\right)\left(\xi_{ilm} - \xi_{blm}\right) \tag{4}$$

Note that the fractional volume $f_{is}(v)$ of subspecies i is a function of the normalized volumetric size v and $f_{is}(v)$ carries information regarding the size distribution.

2.2. *Expressions for Effective Permittivities*

The condition of secular elimination $\langle \bar{\bar{\xi}}(\bar{r}) \rangle = 0$ is imposed to derive the auxiliary uniaxial permittivity tensor $\bar{\epsilon}_g = diag(\epsilon_{g\rho}, \epsilon_{g\rho}, \epsilon_{gz})$. For scatterers preferentially aligned in the vertical direction and random in azimuth, the orientation of ellipsoidal scatterers is characterized with relative azimuthal angle α between the local and global coordinates. Thus $\langle \bar{\bar{\xi}}(\bar{r}) \rangle$ is simply

$$\langle \bar{\bar{\xi}}(\bar{r}) \rangle = \frac{1}{2\pi} \int_0^{2\pi} d\alpha\, \bar{\bar{T}}^{-1} \cdot \left[f_b \bar{\bar{\xi}}_b + \sum_{i=1}^{N} f_{is} \bar{\bar{\xi}}_i \right] \cdot \bar{\bar{T}} = 0 \tag{5}$$

where the ucm-zero elements of $\bar{\bar{T}}$ arc $T_{11} = T_{22} = \cos\alpha, T_{12} = -T_{21} = \sin\alpha$, and 2'33 = 1. Carrying out the integration over azimuthal angle α yields

$$\sum_{i=1}^{N,b} f_{is} \left(\xi_{ix'} + \xi_{iy'}\right) = 0 \tag{6a}$$

$$\sum_{i=1}^{N,b} f_{is} \xi_{iz'} = 0 \tag{6b}$$

where the summation is over all constituents in the medium including the background whose fractional volume notation $f_{bs} \equiv f_b$ *is* used here for convenience. In *(6)*, ξ's are related to S's and arc expressed in the local coordinates as

$$\xi_{ix'x'}(\epsilon) \equiv \xi_{ix'}(\epsilon) = \frac{\epsilon - \epsilon_{g\rho}}{\epsilon_0 + S_{ix'}(\epsilon - \epsilon_{g\rho})} \tag{7a}$$

$$\xi_{iy'y'}(\epsilon) \equiv \xi_{iy'}(\epsilon) = \frac{\epsilon - \epsilon_{g\rho}}{\epsilon_0 + S_{iy'}(\epsilon - \epsilon_{g\rho})} \tag{7b}$$

$$\xi_{iz'z'}(\epsilon) \equiv \xi_{iz'}(\epsilon) = \frac{\epsilon - \epsilon_{gz}}{\epsilon_0 + S_{iz'}(\epsilon - \epsilon_{gz})} \tag{7c}$$

w ıcre i is 1 ,2,..., AT for the scatterer subspecies or i is replaced by b for the background. In (7), ϵ takes on the value of ϵ_{is} in a scatterer of subspecies i or ϵ_b in the background medium.

The dyadic coefficient $\overline{\overline{S}}_i$ for the ellipsoidal scat t crer is deri ved from t he vanishing condition of the frequency independent terms in the effective scatterer tensor [*Tsang and Kong, 1981 a].* By cancelling the frequency independent terms [in (14)-(16) below], the results for subspecies i arc

$$S_{ix'} = \int_0^{2\pi} d\alpha \, \frac{\epsilon_0 \gamma_{ix}^2 \cos^2 \alpha}{2\pi \epsilon_{g\rho} a_i \sqrt{a_i}} \left[(1 + a_i) \tan^{-1} \sqrt{a_i} - \sqrt{a_i}\right] \tag{8a}$$

$$S_{iy'} = \int_0^{2\pi} d\alpha \, \frac{\epsilon_0 \gamma_{iy}^2 \sin^2 \alpha}{2\pi \epsilon_{g\rho} a_i \sqrt{a_i}} \left[(1 + a_i) \tan^{-1} \sqrt{a_i} - \sqrt{a_i}\right] \tag{8b}$$

$$S_{iz'} = \int_0^{2\pi} d\alpha \, \frac{\epsilon_0 (1 + a_i)}{2\pi \epsilon_{gz} a_i \sqrt{a_i}} \left[\sqrt{a_i} - \tan^{-1} \sqrt{a_i}\right] \tag{8c}$$

where the integrations over α arc carried out numerically. The quantities a_i, γ_{ix}, and γ_{iy} arc

$$a_i = \alpha_\epsilon \gamma_i^2 - 1, \quad \alpha_\epsilon = \frac{\epsilon_{gz}}{\epsilon_{g\rho}} \tag{9a}$$

$$\gamma_i = \frac{1}{\ell_{iz'}} \left(\frac{\cos^2 \alpha}{\ell_{ix'}^2} + \frac{\sin^2 \alpha}{\ell_{iy'}^2} \right)^{-\frac{1}{2}} \tag{9b}$$

$$\gamma_{ix} = \frac{1}{\ell_{ix'}} \left(\frac{\cos^2 \alpha}{\ell_{ix'}^2} + \frac{\sin^2 \alpha}{\ell_{iy'}^2} \right)^{-\frac{1}{2}} \tag{9c}$$

$$\gamma_{iy} = \frac{1}{\ell_{iy'}} \left(\frac{\cos^2 \alpha}{\ell_{ix'}^2} + \frac{\sin^2 \alpha}{\ell_{iy'}^2} \right)^{-\frac{1}{2}} \tag{9d}$$

With the above results for $\overline{\overline{S}}_i$, the average dyadic coefficient $\langle\overline{\overline{S}}\rangle$ in (1) is determined by

$$\langle\overline{\overline{S}}\rangle = \sum_{i=1}^{N,b} \frac{f_{is}}{2\pi} \int_0^{2\pi} d\alpha\, \overline{\overline{T}}^{-1} \cdot \begin{bmatrix} S_{ix'} & 0 & 0 \\ 0 & S_{iy'} & 0 \\ 0 & 0 & S_{iz'} \end{bmatrix} \cdot \overline{\overline{T}}$$

$$= \sum_{i=1}^{N,b} \frac{f_{is}}{2} \begin{bmatrix} S_{ix'} + S_{iy'} & 0 & 0 \\ 0 & S_{ix'} + S_{iy'} & 0 \\ 0 & 0 & 2S_{iz'} \end{bmatrix} = \begin{bmatrix} S_\rho & 0 & 0 \\ 0 & s & 0 \\ 0 & 0 & s, \end{bmatrix} \tag{lo}$$

for $\overline{\overline{S}}_b = \sum_{i=1}^{N} f_i \overline{\overline{S}}_i /(1 - f_b)$. Then ϵ_g's and S'S are solved iteratively from the above equations.

To complete the derivation of the effective permit tivity tensor, the effective scatterer tensor needs to be obtained. Due to the azimuthal symmetry, the effective scatterer tensor $\overline{\overline{\xi}}_{eff}$ takes on the uniaxial form

$$\overline{\overline{\xi}}_{eff} = \begin{bmatrix} \xi_{eff\rho} & 0 & 0 \\ 0 & \xi_{eff\rho} & 0 \\ 0 & 0 & \xi_{effz} \end{bmatrix} \tag{11}$$

which is defined by (2) from which the following results

$$\xi_{eff\rho} = \frac{1}{2} \sum_{i=1}^{N} \int_{v_i} dv\, [\delta_{i\xi x'} (I_{ix'} + S_{ix'}) + \delta_{i\xi y'} (I_{iy'} + S_{iy'})] \tag{12a}$$

$$\xi_{effz} = \sum_{i=1}^{N} \int_{v_i} dv\, \delta_{i\xi z'} (I_{iz'} + S_{iz'}) \tag{12b}$$

The variance $\delta_{i\xi}$'s in (12) are related to fractional volumes and local scatterers by

$$\delta_{i\xi j'} = f_{is} f_b (\xi_{ij'} - \xi_{bj'}) (\xi_{ij'} - \xi_{bj'}) \tag{13}$$

The quantities $I_{ix'}, I_{iy'}$, and $I_{iz'}$ in (12) are derived by substituting elements of the anisotropic dyadic Green's function [*Nghiem et al., 1990*] and the Fourier transform (3)

of the normalized correlation function in (2). The complex variable integrations involve only elementary functions. The results that follow contain square root and inverse tangent functions of complex arguments. For the square root ($\sqrt{w}$) of a complex number w, there are two Riemann sheets and the value on the principal Riemann sheet is chosen with the branch cut on tile negative real axis of the complex plane such that, $-\pi < \arg w \leq \pi$ for theargument Of w. The inverse tangent function of a complex number w is determined by $\tan^{-1} w = 1/(2i)\ln[(1+iw)/(1-iw)]$ which has an infinite number of Riemann sheets and the value of the: natural logarithm is taken on the principal Riemann sheet with the branch cut also along the negative real axis such that $-\pi < \arg[(1+iw)/(1-iw)] \leq \pi$. Figure 3 shows a schematic visualization of these Riemann sheets. The sheets should collapse onto the complex plane and their limits extend to the entire complex plane including zero for the square root and excluding zero for the logarithm. With these single-value complex functions, the results for I's of subspecies i arc:

(a) For z' element

$$I_{iz'} = -\int_0^{2\pi} d\alpha \, \frac{\epsilon_0}{\pi \epsilon_{gz'}} (\mathcal{I}_s + \mathcal{I}_d) \tag{14a}$$

$$\mathcal{I}_s = -\frac{\alpha_\epsilon \gamma_i^2 \sqrt{\alpha_\epsilon \gamma_i^2}}{2a_i^2} \left[\frac{\sqrt{-\zeta}}{\vartheta_e} + \frac{\vartheta_e + \zeta}{\vartheta_e \sqrt{\vartheta_e}} \left(\frac{\pi}{2} - \tan^{-1} \frac{\sqrt{-\zeta}}{\sqrt{\vartheta_e}} \right) \right] \tag{14b}$$

$$\mathcal{I}_d = \frac{\alpha_\epsilon \gamma^2}{2a_i^2} \left[\frac{1 + a_i \nu_{gz'}^2}{\vartheta_o} + \frac{\vartheta_o (a_i + 2) - (b + a_i \nu_{gz'}^2)}{\vartheta_o \sqrt{\vartheta_o}} \left(\frac{\pi}{2} - \tan^{-1} \frac{1}{\sqrt{\vartheta_o}} \right) \right] \tag{14c}$$

$$\nu_{gz'}^2 = k_{g\rho}^2 \ell_{iz'}^2 , \quad k_{g\rho}^2 = \omega^2 \mu_0 \epsilon_{g\rho} , \quad \zeta = \alpha_\epsilon \gamma_i^2 \nu_{gz'}^2 \tag{14d}$$

$$b = \frac{\alpha_\epsilon \gamma_i^2 + \zeta}{a_i} , \quad \vartheta_o = b - 1 , \quad \vartheta_e = b + \zeta \tag{14e}$$

(b) For x' element

$$I_{ix'} = \int_0^{2\pi} d\alpha \, \frac{k_0^2}{\pi} \left(\ell_{iy'}^2 \gamma_{iy}^4 \sin^2\alpha \; I_o + \ell_{ix'}^2 \gamma_{ix}^4 \cos^2\alpha \; I_e \right) \tag{15a}$$

$$I_e = \alpha \left[(\mathcal{I}_1^e - \mathcal{I}_2^e - \mathcal{I}_3^e) + \frac{1}{\zeta} \left(\mathcal{I}_s + \mathcal{I}_d - \frac{1}{2} \right) \right] \tag{15b}$$

$$I_o = \mathcal{I}_1^o - \mathcal{I}_2^o - \mathcal{I}_3^o \tag{15c}$$

$$\mathcal{I}_1^e = \frac{\alpha_\epsilon \gamma_i^2 \sqrt{\alpha_\epsilon \gamma_i^2}}{2 a_i^2 \vartheta_e} \left[-\frac{\sqrt{-\zeta}}{b} + \frac{1}{\sqrt{\vartheta_e}} \left(\frac{\pi}{2} - \tan^{-1} \frac{\sqrt{-\zeta}}{\sqrt{\vartheta_e}} \right) \right] \tag{15d}$$

$$\mathcal{I}_2^e = \frac{1}{2 a_i \vartheta_o} \left[1 - \frac{1}{\sqrt{\vartheta_o}} \left(\frac{\pi}{2} - \tan^{-1} \frac{1}{\sqrt{\vartheta_o}} \right) \right] \tag{15e}$$

$$\mathcal{I}_3^e = \frac{\alpha_\epsilon \gamma_i^2}{2 a_i^2 \vartheta_o} \left[-\frac{1}{b} + \frac{1}{\sqrt{\vartheta_o}} \left(\frac{\pi}{2} - \tan^{-1} \frac{1}{\sqrt{\vartheta_o}} \right) \right] \tag{15f}$$

$$\mathcal{I}_1^o = \mathcal{I}_1^e(\alpha_\epsilon = 1), \quad \mathcal{I}_2^o = \mathcal{I}_2^e(\alpha_\epsilon = 1), \quad \mathcal{I}_3^o = \mathcal{I}_3^e(\alpha_\epsilon = 1) \tag{15g}$$

(c) For y' element

$$I_{iy'} = \int_0^{2\pi} d\alpha \, \frac{k_0^2}{\pi} \left(\ell_{ix'}^2 \gamma_{ix}^4 \cos^2\alpha \; I_o + \ell_{iy'}^2 \gamma_{iy}^4 \sin^2\alpha \; I_e \right) \tag{16}$$

Substituting $\bar{\bar{\epsilon}}_g$, $\langle \bar{\bar{S}} \rangle$, and $\bar{\bar{\xi}}_{eff}$ in (1) finally yields the uniaxial effective permittivity tensor $\bar{\bar{\epsilon}}_{eff} = diag(\epsilon_{eff\,\rho}, \epsilon_{eff\,\rho}, \epsilon_{eff\,z})$ whose lateral and vertical elements are, respectively

$$\epsilon_{eff\,\rho} = \epsilon_{g\rho} + \epsilon_0 \xi_{eff\,\rho} / (1 - S_\rho \xi_{eff\,\rho}) \tag{17a}$$

$$\epsilon_{eff\,z} = \epsilon_{gz} + \epsilon_0 \xi_{eff\,z} / (1 - S_z \xi_{eff\,z}) \tag{17b}$$

Depending on medium structures and characteristics, size and shape distributions can be measured with digitized section images [*Vallese and Kong, 1981; Perovich and Richter-Menge, 1994].* Local correlation lengths corresponding to a scatterer can also be estimated by setting the correlation volume to be equal to the volume of the scatterer with the same axial ratios [*Yueh* et *al., 1990].* For an ellipsoid with semi-axes a, b, and c, the relations with correlation lengths are

$$\ell_{ix'} \ell_{iy'} \ell_{iz'} = cba/6, \quad \ell_{iy'}/\ell_{ix'} = b/c, \quad \ell_{iz'}/\ell_{ix'} = a/c \tag{18}$$

The expressions in (17) indicate that the effective permittivity tensor $\bar{\bar{\epsilon}}_{eff}$ is anisotropic with an optic axis in the vertical direction due to the preference in the orientation distribution, The above derivation has been carried out for ellipsoidal scatterers with arbitrary axial ratios, which can be reduced to the case of spheroidal or spherical scatterers.

3. APPLICATION TO SEA ICE

The results derived in the previous sections are now specifically applied to model sea ice including thermodynamic phase distribution and structural met amorphism. Sea ice is a multiphase mixture as illustrated in Figure 1. The background is ice grown in the columnar form as observed in congelation ice. In many cases, crystallographic c-axes in sea ice arc parallel to the horizontal plane. When there is no directional stress, such as caused by a sea current, exerted during the growth process, the c-axes are randomly oriented in azimuthal directions. Ice platelets in sea ice sandwich saline water from the sca in ellipsoidal pockets called brine inclusions. In addition, there are air bubbles embedded in the ice. When the temperature changes, the solid, liquid, and gaseous phases redistribute, ice structure metamorphoses, and characteristics of constituents in sea ice such as permittivity also vary. Further details of sea ice characteristics can be found in several references [e.g., *Weeks and Ackley, 1982; Nghiem et al. 1995a].*

9.1. Size Distribution

Due to the high permittivity of the saline water at microwave frequencies, brine inclusions have a strong effect on the electromagnetic properties of sea ice. The size

distribution of the inclusions has been reported to follow the power law [*Perovich and Gow*, 1991]. Consider a power-law distribution for number density n of scatterers with size v described by

$$n = n_0 v^{-2p} \tag{19}$$

where p is the power-law index and n_0 is the number density of brine inclusions of the smallest size. The normalized volumetric size has been defined in subsection 2.1 as the ratio of volume v_s of an inclusion over volume v_{s0} of the smallest, one. By definition,

$$v \equiv \frac{v_s}{v_{s0}} = \frac{f_s}{n v_{s0}} \tag{20}$$

in which f_s (let's temporarily drop subscript i for the subspecies) is the fractional volume of inclusions with volume v_s. From (20), the size distribution can also be represented by the fractional volume as

$$f_s(v) = n_0 v_{s0} v^{1-2p} = f_{s0} v^{1-2p} \tag{21}$$

for the fractional volume f_{s0} of inclusions having the smallest size. The size distribution is specified when f_{s0} and p are determined. This can be done if the total fractional volume and t hc minimum, average, and maximum sizes of t hc inclusions are measured.

First, a solution for power-law index p is considered, Average normalized volumetric size v_a is obtained by measuring the size of every inclusion and then taking the average. Mathematically, this process is described by

$$v_a = \frac{1}{f_{sM} - f_{s0}} \int_{f_{s0}}^{f_{sM}} df_s\, v(f_s) = \frac{1}{f_{sM} - f_{s0}} \int_{f_{s0}}^{f_{sM}} df_s \left(\frac{f_s}{f_{s0}}\right)^{1/(1-2p)} \tag{22}$$

The integration ranges from the fractional volume f_{s0} of the smallest inclusions to f_{sM} of the largest. Another method of measuring the average normalized volumetric size is to take

the ratio of total fractional volume f_{sT} to the total number density n_T of the inclusions and normalize it to the smallest volume v_{s0}; i.e.,

$$v_a = \frac{f_{sT}}{n_T v_{s0}} \tag{23a}$$

The total number density n_T is calculated by an integration over the size distribution

$$n_T = \int_1^{v_M} dv n(v) = \int_1^{v_M} dv n_0 v^{-2p} \tag{23b}$$

in which $v_M = v_{sM} / v_{s0}$ is the normalized volumetric size of the largest inclusions. Both (22) and (23) give the same result for average volumetric size v_a

$$v_a = \frac{1-2p}{2(1-p)} \frac{v_M^{2(1-p)} - 1}{v_M^{(1-2p)} - 1}, \qquad \text{for } p \neq \frac{1}{2} \tag{24}$$

This is rearranged to solve iteratively for the power-law index p from

$$p = \frac{1}{2 \ln v_M} \ln\left(\frac{v_a - q v_M}{v_a - q}\right) + \frac{1}{2}, \quad \text{with} \quad q = \frac{1-2p}{2(1-p)} \tag{25}$$

The following conditions arc used to check the convergence of the solution

$$v_a = q \frac{v_M^{2(1-p)} - 1}{v_M^{(1-2p)} - 1} \tag{26a}$$

$$v_M = \left(\frac{v_a - q}{v_a - q v_M}\right)^{1/(1-2p)} \tag{26b}$$

Note that the right hand side of *(24)* has to be positive since v_a is positive. Furthermore, $v_M > 1$ results in

$$\frac{v_M^{2(1-p)} - 1}{v_M^{(1-2p)} - 1} > 0 \quad \Rightarrow \quad \frac{1-2p}{2(1-p)} > 0 \tag{27}$$

which imposes the condition $p \in (0.5, 1)$. Thus, the power-law index p is determined if v_a and v_M are known. For given v_a and v_M, if the solution for p is not possible, a different description of the size distribution should be considered.

Now, fractional volume f_{s0} of the smallest inclusions needs to be derived to complete the determination of the size distribution. Total fractional volume f_{sT} of the inclusions is calculated by integrating the fractional volume distribution over the entire size range

$$f_{sT} = \int_1^{v_M} dv\, f_s(v) = f_{s0} \frac{v_M^{2(1-p)} - 1}{2(1-p)}, \qquad \text{for } p \neq 1 \tag{28}$$

When the total fractional volume is known from measured data, f_{s0} is solved by using (28) and the solution for the power-law index p.

The size distribution changes with temperature. When the temperature varies, volumes of individual brine inclusions do also. Assume that the volumes of the inclusions change at the same rate; i.e., for two different temperatures T_0 and T,

$$\frac{Z),(TO)}{v_{s0}(T_0)} = \frac{v_s(T)}{v_{s0}(T)} \tag{29}$$

Also assume that no new inclusion is created nor existing ones removed at different temperatures; i.e., the density number of the inclusions is conserved. This condition requires

$$\frac{f_s(T_0)}{v_s(T_0)} = \frac{f_s(T)}{v_s(T)} \quad \text{and} \quad \frac{f_{s0}(T_0)}{v_{s0}(T_0)} = \frac{f_{s0}(T)}{v_{s0}(T)} \tag{30}$$

Let the size distribution at temperature T_0 conform to a power law with index $p(T_0)$ so that

$$f_s(T_0) = f_{s0}(T_0)\, v^{1-2p(T_0)} \tag{31}$$

Substituting (31) in (30) renders

$$\frac{f_s(T)}{v_s(T)} = \frac{f_{s0}(T_0)}{v_s(T_0)}\, v^{1-2p(T_0)} \tag{32}$$

From (29), (30), and (32), it is shown that

$$f_s(T) = f_{s0}(T)\, v^{1-2p(T_0)} \tag{33}$$

Equation (33) indicates that the power-law index does not change as the temperature varies when the above assumptions arc reasonable. Under tile above conditions, volumetric sizes are also preserved at different temperatures so that v.(T) = $v_a(T_0)$ and $v_M(T) = v_M$ (T.). If ice structural data are not available at all temperatures under consideration, the index obtained at a temperature may be used at a different, temperature when there is no severe brine loss nor ice deformation. otherwise, thin section images arc necessary to determine the size distribution. For air bubbles, the size distribution is obtained in the same manner.

9.2. *Shape Distribution*

Shapes of brine inclusions have been observed as substantially ellipsoidal [e.g., Gow *et al.,1987*]. From thin sections of saline ice grown at the U.S. Army Cold Regions Research and Engineering Laboratory [Gow *et al., 1987*], it is seen that only inclusions of small sizes have a more rounded spheroidal form. Following these observations, a s1ow1 y varying logarithmic function is used to describe the shape distribution such that

$$co(v) = (e_{aM} - e_{am})\frac{\ln v}{\ln v_M} + e_{am} \tag{34a}$$

$$e_b(v) = (e_{bM} - e_{bm})\frac{\ln v}{\ln v_M} + e_{bm} \tag{34b}$$

where the axial ratios $e_a = a/c$ and e_b = b/c. Subscript M and m are for maximum and minimum values, respectively. This shape distribution implies that inclusions are substantially ellipsoidal for large and medium size and more rounded for small sizes.

When the temperature increases during a warming cycle, the shapes of the inclusions become less ellipsoidal or more rounded as seen in thin sections of saline ice prepared by Gow et al. [*1987*]. This thermal effect on the sea ice structure is modeled with a reshaping

factor operating on axial ratios e_{aM} and e_{bM}. Suppose that axial ratio $e_{bM}(T_0)$ at the low temperature T_0 becomes $e_{bM}(T_h)$ at the highest temperature T_h of the thermal cycle. The axial ratio at temperature T between T_0 and T_h then assumes the form

$$e_{bM}(T) = [e_{bM}(T_0) - e_{bM}(T_h)]\,\frac{1 - \exp[P(T - T_h)]}{1 - \exp[P(T_0 - T_h)]} + e_{bM}(T_h) \tag{35a}$$

where P is the reshaping index and all temperatures are in degrees Celsius below the freezing point. When the thermal cycle has a large temperature range, (35a) can be approximated as

$$e_{bM}(T) = [e_{bM}(T_0) - e_{bM}(T_h)]\,\{1 - \exp[P(T - T_h)]\} + e_{bM}(T_h) \tag{35b}$$

such that the value of $e_{bM}(T)$ is well preserved near temperature T_0. Similar formulas apply to e_{aM}. This thermal process describes a structural metamorphism which makes ellipsoidal shapes of the inclusions transform into a more rounded form with an increasing temperature. For air bubbles, observed shapes are rather rounded in the form of spheroids or spheres [*Perovich and Gow, 1991; Gow et al. 1987*]. Therefore, shapes of air bubbles do not change as much as those of brine inclusions and are assumed to be unaffected by thermal variations.

3.3. Correlation Lengths

When scatterer axial lengths are specified, the corresponding correlation lengths in the local coordinates can be calculated from (18). Furthermore, correlation lengths also vary as a function of temperature since sizes and shapes of the inclusions change with temperature. If geometrical measurements of the scatterers are made at temperature To,

correlation lengths at a different temperature, 2', may be estimated under the assumptions in subsection 3.1. From (30), the normalized volumetric size at temperature T can be written as

$$v_s(T) = \frac{f_s(T)}{f_s(T_0)} v_s(T_0) \tag{36}$$

The size distributions at different temperatures in (31) and (33) and total fractional volume f_{sT} given by *(28)* lead to the relation

$$\frac{f_s(T)}{f_s(T_0)} = \frac{f_{s0}(T)}{f_{s0}(T_0)} = \frac{f_{sT}(T)}{f_{sT}(T_0)} \tag{37}$$

Relation (36) and the ratios in (37) together with the definition of normalized volumetric size (20) give

$$v_s(T) = \frac{v f_{s0}(T)}{f_{s0}(T_0)} v_{s0}(T_0) \tag{38}$$

Volume v,(T) and $v_{s0}(T_0)$ of an ellipsoidal inclusion are calculated from the sizes as

$$v_s(T) = \frac{4\pi}{3} e_a(T) e_b(T) c^3(T) \tag{39a}$$

$$v_{s0}(T_0) = \frac{4\pi}{3} e_{am}(T_0) e_{bm}(T_0) c_m^3(T_0) \tag{39b}$$

where m denotes the minimum. Substituting (39) in (38) and using (18) render the local correlation lengths corresponding to the inclusion

$$\ell_{x'}(T) = \frac{v f_{s0}(T)}{6 f_{s0}(T_0)} \frac{e_{am}(T_0) e_{bm}(T_0)}{e_a(T) e_b(T)}^{\frac{1}{3}} c_m(T_0) \tag{40a}$$

$$\ell_{y'}(T) = e_b(T) \ell_{x'}(T) \ , \quad \ell_{z'}(T) = e_a(T) \ell_{x'}(T) \tag{40b}$$

These equations determine the correlation lengths at temperature T from measurements at temperature *To.* In (40a), ratio $f_{sT}(T)/f_{sT}(T_0)$ can be used instead of $f_{s0}(T)/f_{s0}(T_0)$ according to (37). Correlation lengths for air bubbles can be obtained in the same manner.

3.4. Constituent Characteristics

The ordinary ice polymorph I_h with a hexagonal symmetry (as distinguished from I_c with a cubic symmetry) is predominant in natural geophysical conditions [*Hobbs, 1974; Glen, 1974; Weeks and Ackley, 1982; Petrenko, 199,?]*. The principal hexagonal axis is the crystallographic c-axis. Each polycrystal in congelation columnar sea ice consists of ice platelets perpendicular to the c-axes. During the growth process, ice entraps sea water in ellipsoidal pockets, referred to as brine inclusions, between the ice platelets. In columnar ice, c-axes become parallel to within a few degrees of the horizontal plane [*Weeks and Ackley, 1982*] and brine inclusions are therefore oriented preferentially in the vertical direct ion.

Sea icc is naturally a multiphase mixture consisting of solid ice, liquid brine, and gaseous inclusions. While the real part of ice permittivity is not very sensitive to temperature, the imaginary part is dispersive and varies significantly with temperature. Empirical formulas to calculate ice permittivity as a function of temperature at microwave frequencies are available [*Vant et al., 1982; Tiuri et al., 1984; Mätzler and Wegmüller, 1987*]. The magnitudes of complex permittivity of brine in sea ice are large compared to those of ice, and both real and imaginary parts decrease several times as frequency increases. Empirical formulas to compute complex dielectric constants of brine were reported by Stogryn and Desargant [1985] in terms of temperature and microwave frequency.

Constituent phases in sea ice are interrelated thermodynamically, When the temperature of sea ice varies, the fractional volume of brine inclusions and air bubbles changes accordingly. On the basis of phase equilibrium, Cox and Weeks [1989] provided equations

for determining fractional volumes of brine inclusions and air bubbles n sea ice in the temperature range of –2° C to – *30° C.* The required input parameters are bulk ice density, salinity, and temperature. While the volume of solid salt is usually minute and has a negligible direct contribution to effective permittivities, the process of salt expulsion is important due to the consequential redistribution of the phases of brine and air inclusions. The salt Na_2SO_4 $10H_2O$ crystallizes at –8.2° C; however, the phase change is much sharper at –21. 1°C. This is the eutectic temperature of $NaCl \cdot 2H_2O$ corresponding to the precipitation of the salt (sodium chloride dihydride). In sea water brine, an initial formation of the salt appears at —22.9° C [*Weeks and Ackley, 1982*]. This phase transition causes a kink in the phase curves and impacts the effective permittivities of sea ice as a function of temperature.

4. DATA COMPARISON AND DISCUSSION

In this section, results calculated from the model are compared with experimental data. Complex permittivities of sea ice grown from saline water at the U.S. Army Cold Regions and Research Engineering Laboratory (CRREL) were determined [*Arcone et al., 1986].* The ice slab was composed of columnar ice crystals exhibiting the ice plate/brine layer substructure that characterizes congelation sea ice in the Arctic [*Arcone et* al., *1986*]. The permittivities were obtained from transmission measurements for waves normally incident on the ice slab; therefore, only data for $\epsilon_{eff\,\rho}$ corresponding to an ordinary wave were reported; the extraordinary component was not available for the study in this section. Uncertainties due to data variations and theoretical assumptions are also assessed

with sensitivity analyses.

4. 1. Ice Characterization

The sca ice slab was taken from a saline ice sheet (Sheet 85-3 [*Arcone et al., 1* 986]) to a laboratory environment where the temperature was controllable. Measurements were made at temperature intervals during progressive warming of the ice slab from –32° C to –2° C at a C-band frequency of 4.8 GHz. The salinity was 5.4 $^0/_{00}$ before testing ancl reduced to 4.2 $^0/_{00}$ after testing clue to brine loss during the warming process. Only the final bulk ice density of 0.866 Mg/m^3 was reported. For a given set of temperature, salinity, ice density, and wave frequency, fractional volumes and permittivities of the constituents in sea ice are calculated from the empirical formulas as discussed in section 6.4. Typically in these cases, total fractional volumes of brine inclusions ant{ air bubbles are on the order of 10%. Real parts of the relative permittivities of the ice background are about 3.15 and imaginary parts are on the order of 0.001. Both the real and imaginary parts of brine permittivities arc about one order of magnitude nigher than the real parts of the ice background relative permittivities.

For ice structure, dendritic planes normal to c-axes show a marginal tilt of only 2°-4° and can be modeled approximately as vertical. Photographs of horizontal thin sections taken from the ice slab before and after the thermal modification were presented by Gow et al. [1981. It is observed from the photographs that c-axes are randomly oriented in azimuthal directions, Initially at – 30° C, minimum, average, and maximum linear sizes are estimated as 0.05 mm, 0.10 mm, and 0.30 mm, respectively. To calculate the power-law index for brine inclusions, normalized volumetric sizes corresponding to cubics of the ratios of

the above linear sizes are used; this gives the index of 0.8945 for the size distribution, The initial axial ratio e_{bm} for brine inclusions of smallest size is 1 representing the spheroidal shape. The maximum axial ratio e_{bM} is roughly estimated to be 8 to describe the substantially ellipsoidal shape of large inclusions. Vertical section images were also available but not large enough to see substructures of the inhomogeneities; therefore, vertical axial sizes of these scatterers have to be chosen and sensitivity analyses will be done to study related uncertainties. The choice for initial minimum and maximum major axial ratios is e_{am} = 2 and e_{aM} = 10 to cover the range of variations in brine inclusion sizes. After the warming process, axial ratios for brine inclusions are taken to be e_{bM} = 1.5 and e_{aM} = 3 to account for the change from substantially ellipsoidal shapes into rounded forms. The reshaping index can be estimated from (35) when thin section images are available for some intermediate stages in the thermal modification process. Here, a reshaping index of *0.3* is assumed for the validity condition of (35 b).

For air bubbles, the effect on effective permittivities is not as strong as that due to brine inclusions. Air bubbles are much more rounded than brine inclusions. The shape change in air bubbles is therefore not large and the bubbles are considered as spheroids having circular cross sections as observed in the horizontal thin sections, Uniform axial ratios of air bubbles are assumed to be e_b = 1 and e_a = 2, taken after the values observed by Perovich and Gow [1991]. Initial linear sizes of air bubbles are taken to be the same as those of brine inclusions and thus the power-law index is also 0.8945. While the bubble shape is considered unchanged thermally, bubble size variations as a function of temperature are taken into account.

4.2, Data Comparisons

In this subsection, the experimental observations are explained with the theoretical model. The model is first simplified. Then, the complexity is added to arrive at the better description of the medium with the full model. This st[p-by-step method is used to identify physical mechanisms responsible for the behavior of effective permittivity under changing thermal conditions,

First, brine loss during the warming process is ignored and the shape of brine inclusions is considered as uniform with average axial ratios $e_b = 3$ and $e_a = 5$. These ratios are kept constant with respect to temperature. However, size distributions for both brine inclusions and air bubbles are included. Results from the calculation for the imaginary part of relative effective permittivity $\epsilon_{eff\rho}/\epsilon_0$ ($\epsilon_0 = 8.8542 \times 10^{-12} F \cdot m^{-1}$ is the permittivity of free space) are plotted with the dash curve in Figure 4 together with measured data obtained from the experiment. In genera], the theoretical curve shows an increasing trend as temperature increases. This is caused by the increase of brine fractional volume at higher temperat ures. The kink observed at --23° C (calculations are made at intervals of 1° C started from –30° C) corresponds to the phase change associated with the formation of sodium chloride dihydride and the solidification of brine at colder temperatures. The steep slope of the theoretical curve in the higher temperature range is a result of the fast increase in the brine fractional volume. Compared wit h experiment al data, the theoretical values are too low at low temperatures and too high at high temperatures.

The shape distribution of brine inclusions and its variations with temperature are now considered. Brine inclusions are grouped into 20 subspecies; which are sufficient for

a good convergence in the results as compared to test talc.ulatiolls with 100 subspecies. The calculated results arc shown with the dash-dot curve in Figure 4. Compared with the old theoretical results, the new curve is higher at low temperatures and lower at high temperatures. In the low temperature range, higher values are caused by the existence of more substantially ellipsoidal brine inclusions which have stronger depolarization effects and larger cross sections. At higher temperatures, the effect of inclusion rounding are more prominent in the competition with the increasing effect of higher fractional volumes to render the results to lower values. Regarding the experimental data, the comparison is much better except at temperatures higher than - -8° C the calculated results are still larger than the measured values, If the brine loss represented by the decrease in salinity from 5.4 O/oo to 4.2 O/oo is incorporated in the model by a linear decrease in salinity from –8° C to –4° C, the theoretical curve shown in Figure 5a explains all the trends observed in the experimental data for the imaginary part of the relative effective permittivity. The real part is presented in Figure 5b which indicates that the calculated values are within 10% lower than the measured data.

For the cooling cycle, theoretical results and experimental data are compared in Figure 6a for the imaginary part of the relative effective permittivity. In this case, scatterer shapes and their variations are not specified by documented experimental data. To account for this situation, theoretical results are obtained with the upper bound for a completely reversible process of the shape variations and the lower bound for an irreversible process where the shapes ret ain their form once they becom e more rounded after the warming cycle. Calculated average values are shown with open circles and measured data with black circles in Figure 6a. The comparison indicates that theoretical and experimental

results are well overlapped within their range of variations. The real part of the relative effective permittivity during the cooling cycle is shown in Figure 6b where black circles are experimental data. Effects of shape variations are small for the real part and the continuous curve is the average results, which compare very well with the measurements.

The analysis in this subsection is based as much as possible on available ice characterization data. The lack of characterization information has necessitated some assumptions. The uncertainties associated with the assumptions can be estimated with sensitivity analyses in the next subsection.

4.9. *Sensitivity Analyses*

As seen from the model, shape effects on imaginary parts of effective permittivities are important. In Figure 7a, dash-dot curves are computed with axial ratios varied by ±20% from those used in the last subsection for data comparisons. The continuous curve and the data are the same as in Figure 5a plotted here for reference. The results show that the effect of ellipsoidal shapes is most important in the middle range of temperatures. The insensitivity of shapes at –2° C is due to the rounded form of the inclusions and at low temperatures due to low fractional volume of brine. The corresponding variations in the real part of the relative effective permittivity are presented in Figure 7b. The results show the insensitivity of the real part to the changes in axial ratios. In general, deviations caused by the above uncertainty in scatterer shapes are within the spread of measured data.

Another assumption is that the bulk ice density of 0.866 Mg/m^3 has been used in all of the previous theoretical calculations. This value should not be constant as the salinity

changes due to the brine loss. The inaccuracy in density may lead to an uncertainty in the phase distribution of the constituents in sea ice. The sensitivity analysis is carried out by varying the density by $\pm 5\%$. This is to keep the variations within the density value of gas-free sea ice. The results in Figure 8a indicates that the imaginary part is more sensitive to the density at higher temperatures, In this temperature range, a small change in temperature results in a large variation in the fractional volume of brine inclusions [*Cox and Weeks, 1983*]. The resulting variations arc, however, within the measurement fluctuations. With the results in Figure 8b, a comparison to those in Figure 7b suggests that the volumetric composition in sea ice has a stronger effect on the real part.

For the size distribution, the sensitivity is studied, for example, by varying the maximum normalized volumetric size by $\pm 10\%$. The variations affect the power-law index and thus size distributions of brine inclusions and air bubbles. Calculated results indicate a weak sensitivity in this case. This provides some justification for the use of the result in subsection *3.1* to approximate the power-law index when the ice slab has some brine loss. The sensitivity analyses in this subsection indicate that the assumptions are rather reasonable or, at least, do not lead to too large deviations,

5. SUMMARY

This paper presents an electrothermodynamic model of a multiphase anisotropic medium with multiple species and subspecies characterized by changing phase, orientation, size, and shape distributions under thermal effects. Effective permittivities of the medium are derived with the strong permittivity fluctuation approach. The heterogeneous

medium is effectively anisoh-epic due to a preferential alignment in the orientation distribution of ellipsoidal scatterers. The size distribution of scatterers in a species is described in terms of the number density or the fractional volume as a function of normalized volumetric sizes. The shape distribution is considered by grouping scatterers in a species into many subspecies based on the similarity in scatterer shapes.

The formulation is applied to model congelation sea ice consisting of solid ice, liquid brine, and gaseous inclusions. The model accounts for the thermodynamic redistribution of the constituent phases and the metamorphism of the heterogeneous ice structure. Theoretical and experimental results of effective permittivities are compared well for saline ice at 4.8 GHz undergoing warming and cooling cycles. Observed trends in the measured data arc explained with the physical model. Sensitivities of sea ice characterization parameters arc analyzed to estimate uncertainties due to inaccuracies in characterization data and model assumptions. The analyses show that shapes are important to the imaginary parts of effective permittivities and that density variations also affect the real parts.

The model in this paper includes complex thermodynamic processes including structural changes in sea ice subject to thermal effects. However, the model needs to be further developed to account for a more general case where scatterer orientations have preferential alignments in both vertical and horizontal directions. In this case, the heterogeneous medium becomes effectively biaxial such as columnar sea ice with c-axes directed along a persistent underlying sea current.

Acknowledgments. The research described in this paper was carried out by the Jet Propulsion Laboratory, California Institute of Technology, and was sponsored by the

Office of Naval Research (ONR); by the Massachusetts Institute of Technology, under ONR contracts N00014-89-J-1 107 and NOO014-92-J-4098; and by the U. S. Army CRREL under a contract with ONR.

REFERENCES

Arcone, S. A., A. J. Gow, and S. G. McGrew, Structure and dielectric properties at 4.8 and 9.5 GHz of saline ice, *J. Geophys. Rues.*, *91*(C12), 14281-14303, 1986.

Cox, G. F. N., and W. F. Weeks, Equations for determining the gas and brine volumes in sea-ice samples, *J. Glaciol.*, 29(12), 306-316, 1983.

Glen, J. W., *The Physics of Ice, Monogr. Ser.*, Vol. II-C2a, U. S. Army Corps of Engineers, Cold Regions Research and Engineering Laboratory, Hanover, New Hampshire, 1974.

Gow, A. J., S. A. Arcone, and S. G. McGrcw, Microwave and structural properties of saline ice, *Rep.* 87-20, U. S. Army Corps of Engineers, Cold Regions Research and Engineering Laboratory, Hanover, N. H., 1987.

Hobbs, P. V., *Ice Physics*, Clarendon Press, Oxford, 1974.

Mätzler, C., and U. Wegmüller, Dielectric propert ies of fresh-water ice at microwave frequencies, *J. Phys. D: Appl. Phys.*, *20, 1623-1630, 1987.*

Nghiem, S. V., R. Kwok, J. A. Kong, and R. T. Shin, A model with ellipsoidal scatterers for polarimetric remote sensing of anisotropic layered media, *Radio Sci.*, *28(5), 687-703, 1993.*

Nghiem, S. V,, R. Kwok, S. H. Yueh, and M.R. Drinkwater, Polarimetric signatures of

sea ice - Part I: Theoretical model, *J. Geophys. Res.*, in press, 1995a,

Nghiem, S, V., R, Kwok, S. H. Yueh, J. A. Kong, C. C. Hsu, M. A. Tassoudji, and R. T. Shin, Polarimetric scattering from layered media with multiple species of scatterers, accepted for publication in *Radio Sci.*, 1995b.

Petrenko, V. F., *Structure of Ordinary Ice* I_h, *CRREL Rep. 93-25,* U. S. Army Corps of Engineers, Cold Regions Research and Engineering/; Laboratory, Hanover, New Hampshire, 1993.

Sihvola, A. H., and J. A. Kong, Effective permit tivity of dielectric mixtures, *IEEE Trans. Geosci. Remote Sens.*, *26(4), 420-429, 1988.*

Stogryn, A., An analysis of the tensor dielectric constant of sea ice at microwave frequencies, *IEEE Trans. Geosci. Remote Sens.*, *GE-25(2), 147-158,* 1987.

Stogryn, A., and G. J. Desargant, The dielectric properties of brine in sea ice at microwave frequencies, *IEEE Trans. Antennas Propagat.*, *AP-33*(5), *523-532, 1985.*

Tinga, W. R., W. A. G. Voss, and D. F. Blossey, Generalized approach to multiphase dielectric mixture theory, *J. Applied Phys.*, *44(9), 3897-3902, 1973.*

Tiuri, M. E., A. H. Sihvola, E. G. Nyfors, and M. T. Hallikainen, The complex dielectric const ant of snow at microwave frequencies, *IEEE J. Ocean Eng., OE- 9(5), 377-382, 1984,*

Tsang, L., and J. A. Kong, Scattering of electromagnetic waves from random media with strong permittivity fluctuations, *Radio Sci.*, *16*(3), *303-320,* 1981a.

Tsang, L., and J. A. Kong, Application of strong fluctuation random medium theory to scattering from vegetation-like half space, *IEEE Trans. Geosci. Remote Sens.*, *19*(1), *62-69,* 1981b.

Tsang, L., J. A. Kong, and R. W. Newton, Application of strong fluctuation random medium theory to scattering of electromagnetic waves from a half-space of dielectric mixture, *IEEE Trans. Antennas Propagat.*, *30*(2), *292-302, 1982.*

Vallese, F., and J, A. Kong, Correlation function studies for snow and ice, *J. Appl. Phys.*, *52*(8), *4921-4925, 1981.*

Vant, M. R., R. O. Ramseier, and V. Markios, The complex dielectric constant of sea ice at frequencies in the range 0.1-40 GHz, *J. Applied Phys.*, *49(3), 1264-1280, 1978* (also see erratum by Vant et al., *J. Applied Phys.*, *53*(2), 1269, 1982).

Wait, J, R., Complex resistivity of the earth, *Progress in Electromagnetic Research, vol. 1*, chap. 1, ed. by J.A. Kong, pp. 1-173, Elsevier, New York, 1989.

Wait, J. R., Effective electrical properties of heterogeneous earth models, *Radio Sci., 18(1), 19-24, 1983.*

Weeks, W. F., and S. F. Ackley, *The Growth, Structure, and Properties of Sea Ice*, *Monogr. Ser.*, Vol. 82-1, U. S. Army Corps of Engineers, Cold Regions Research and Engineering Laboratory, Hanover, N. H., 1982.

Yueh, H. A., R. T. Shin, and J. A. Kong, Scattering from randomly oriented scatterers with strong permittivity fluctuations, *J. Electromagn. Waves Appl.*, *4(10), 983-1004, 1990.*

Figure Captions

Figure 1. Modeling of a multiphase mixture containing multiple species and subspecies of scatterers such as sea ice.

Figure 2. Eulerian rotation angles α, β, and γ between local coordinates (x', y', z') and global coordinates (x, y, z).

Figure 3. Schematic illustration of Riemann sheets with unshaded surfaces representing principal sheets. For the cases of (a) square root $\sqrt{w}$: the two sheets are connected to *each other* at the branch cut along the negative real axis, $-\pi <$ arg $w \leq \pi$ in the principal sheet, and the black ellipse at the center indicates that zero belongs to both sheets and (b) inverse tangent $\tan^{-1} w = 1/(2i)\ln[(1 + iw)/(1 - iw)]$: one sheet is connect to *the next* one at tile branch cut along the negative real axis, $-\pi <$ arg$[(1 + iw)/(1 - iw)] \leq \pi$ in the principal sheet, and the open ellipse at the center indicates that zero belongs to no sheet. The sheets are drawn with some spatial separation to create the visual effect. The actual sheets should collapse onto the complex plane and their limits extend to infinite values.

Figure 4. Imaginary part of relative effective permittivity: Black circles are for experimental data, dash curve for calculated results based on orientation and size distribution and uniform scatterer shape; and dash- dot curves for calculated results with shape distribution also included.

Figure 5. Relative effective permittivity in warming cycle: (a) Imaginary part and (b)

Real part. Black circles are for experimental data and the continuous curve for calculated results obtained from the complete model,

Figure 6. Relative effective permittivity in cooling cycle: (a) Imaginary part and (b) Real part. Black circles are for experimental data and open circles for calculated results. For the real part, the continuous curve is for calculated results.

Figure 7. Effects of shape variations on (a) imaginary part and (b) real part of relative effective permittivity: Black circles arc for experiment al data, the continuous curve for calculated results, and dash-dot curves for upper and lower bounds obtained by varying the axial ratios by ±20%.

Figure 8. Effects of density variations on (a) imaginary part and (b) real part of relative effective permittivity: Black circles are for experimental data, the continuous curve for calculated results, and dash-dot curves for upper and lower bounds obtained by varying the bulk ice density by ±5%.

AN ANISOTROPIC MULTIPHASE MIXTURE

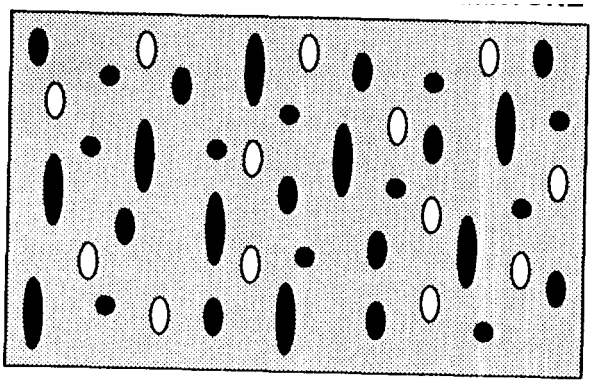

SYMBOL	MODEL	SEA ICE
u	BACKGROUND	SOLID ICE
o	SPECIES	AIR BUBBLES
	SPECIES	LIQUID BRINE
	Subspecies	ELLIPSOIDS
	SUBSPECIES	SPHEROIDS
	SUBSPECIES	SPHERES

FIGURE 1

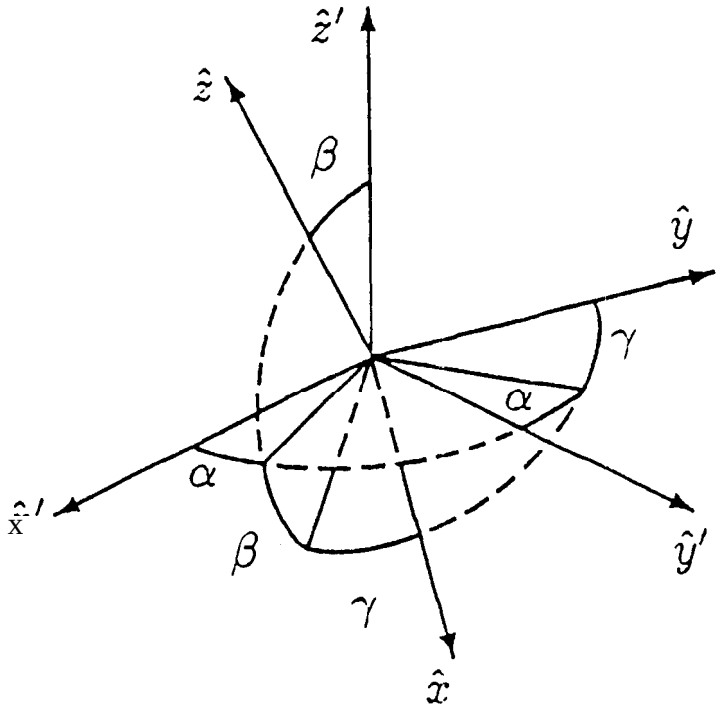
$\hat{z}'$
$\hat{z}$
β
$\hat{y}$
γ
α
α
$\hat{x}'$
β
$\hat{y}'$
γ
$\hat{x}$

FIG. 2

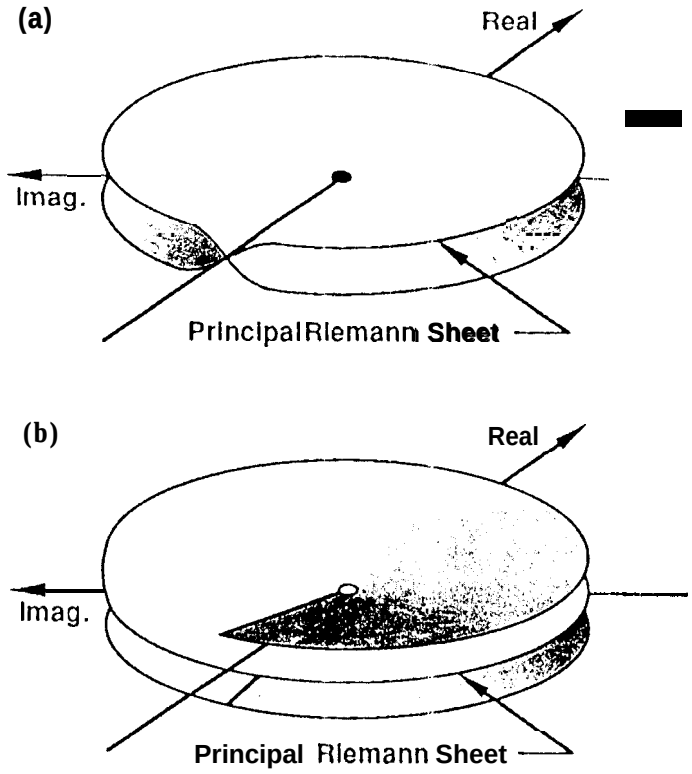
(a)
Real
Imag.
Principal Riemann Sheet
(b)
Real
Imag.
Principal Riemann Sheet

FIGURE 3

FIG. 4

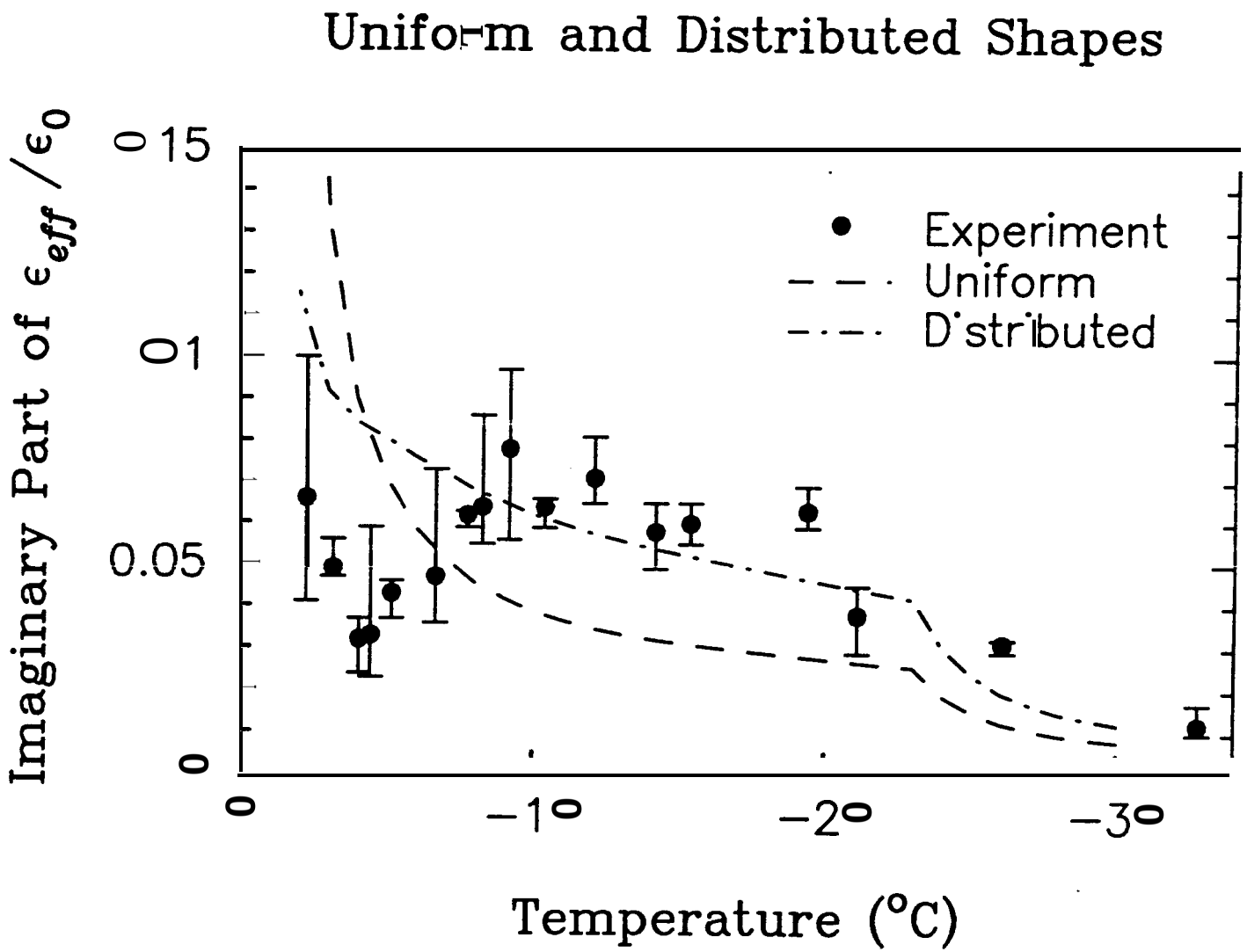
Uniform and Distributed Shapes
Imaginary Part of $\epsilon_{eff}/\epsilon_0$
0.15
0.1
0.05
0
0
−10
−20
−30
Temperature (°C)
Experiment
Uniform
Distributed

nahiem

FIG. 5a

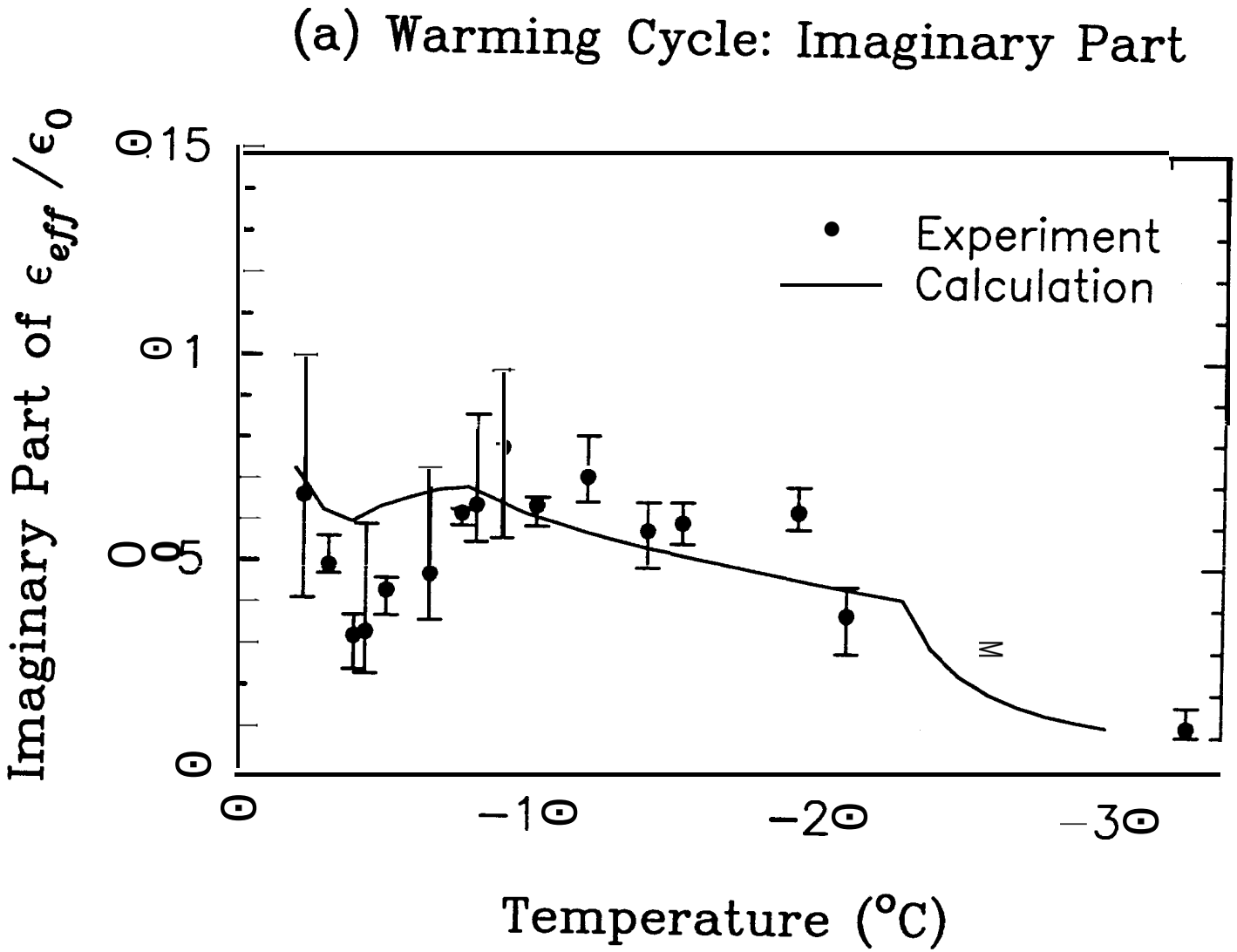
(a) Warming Cycle: Imaginary Part
Imaginary Part of $\epsilon_{eff}/\epsilon_0$
0.15
0.1
0.05
0
0
−10
−20
−30
Temperature (°C)
Experiment
Calculation

FIG. 5b

(b) Warming Cycle: Real Part

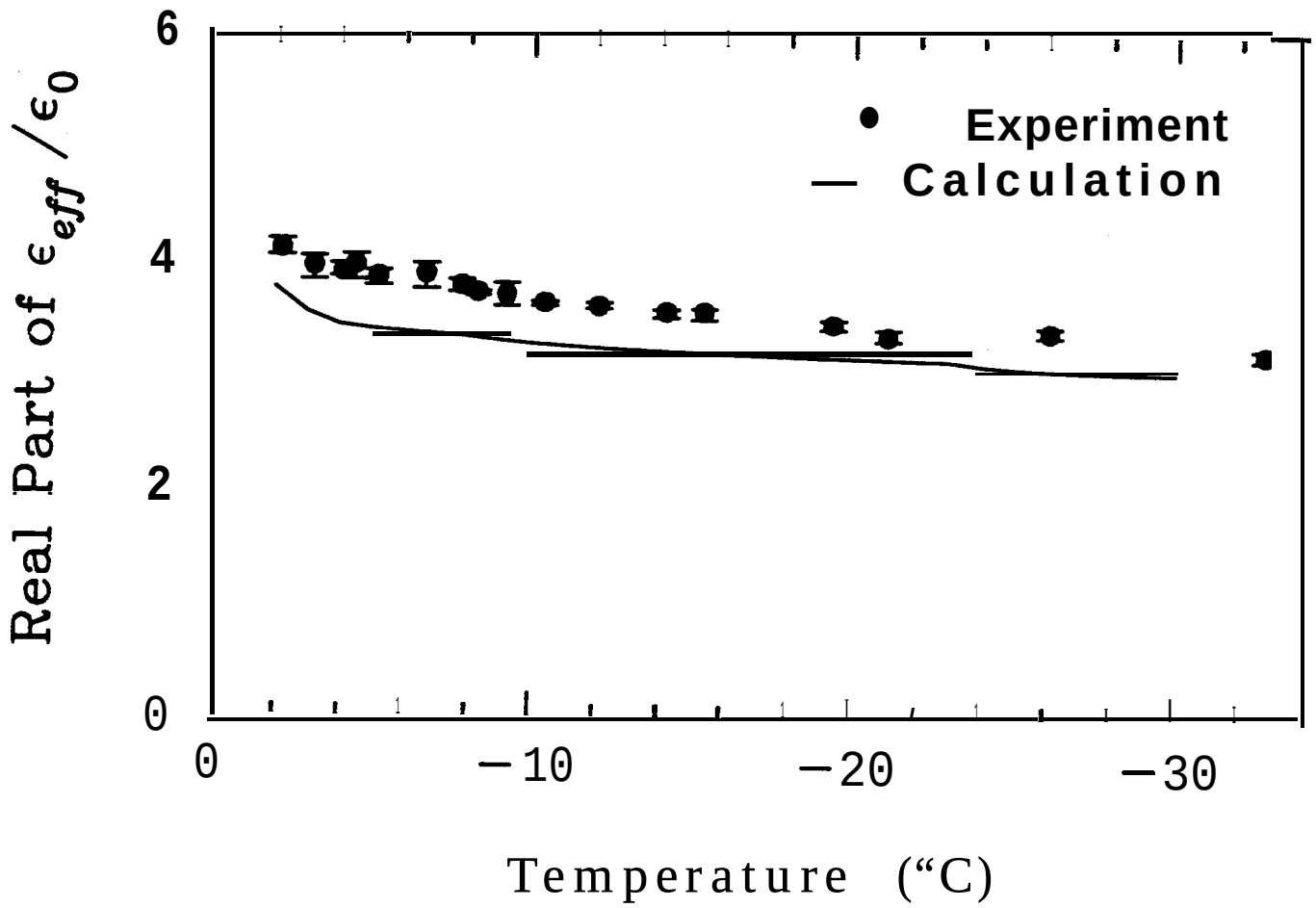

nahiem

FIG. 6a

(a) Cooling Cycle: Imaginary Part

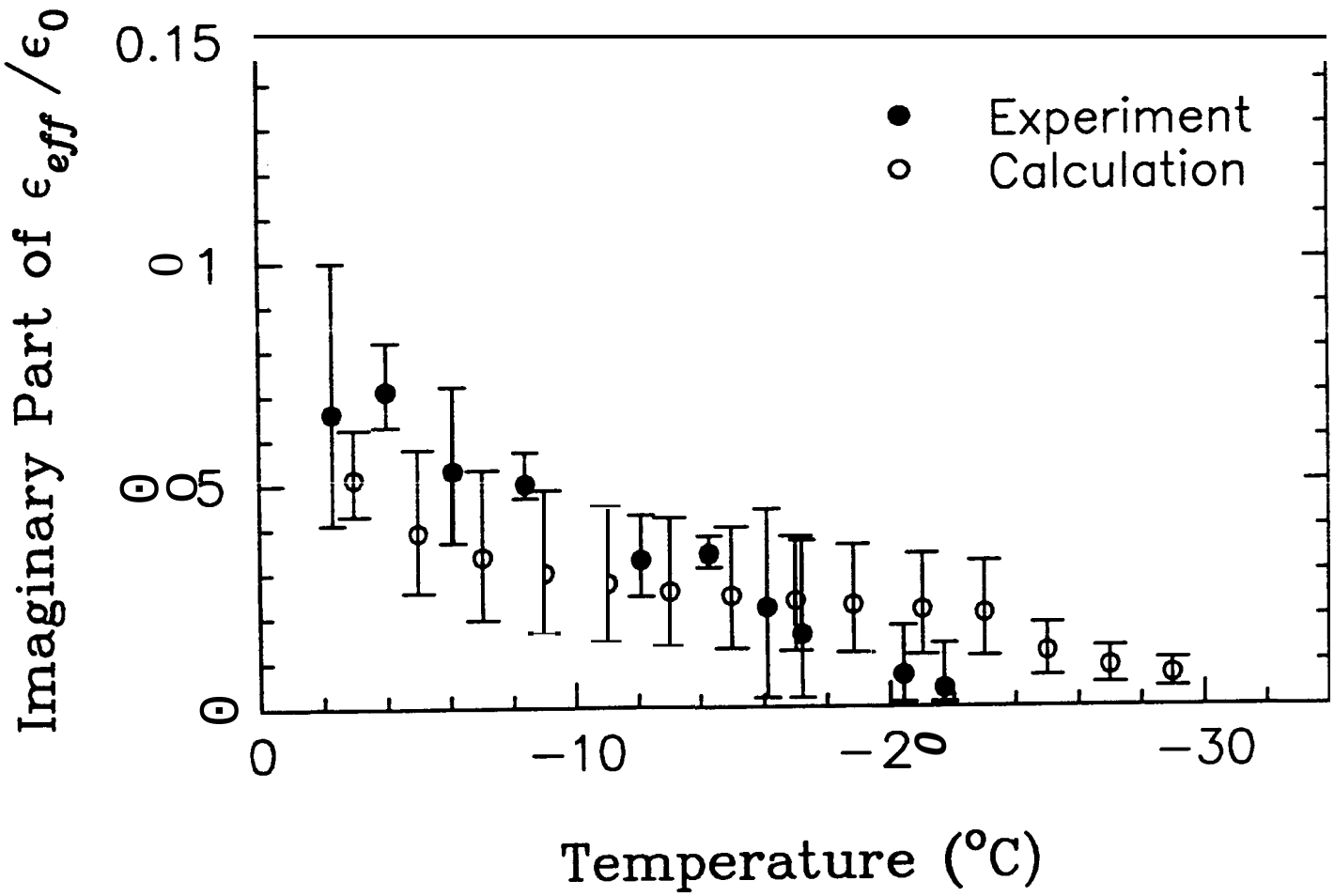

nahiem

FIG, 6b

(b) Cooling Cycle: Real Part

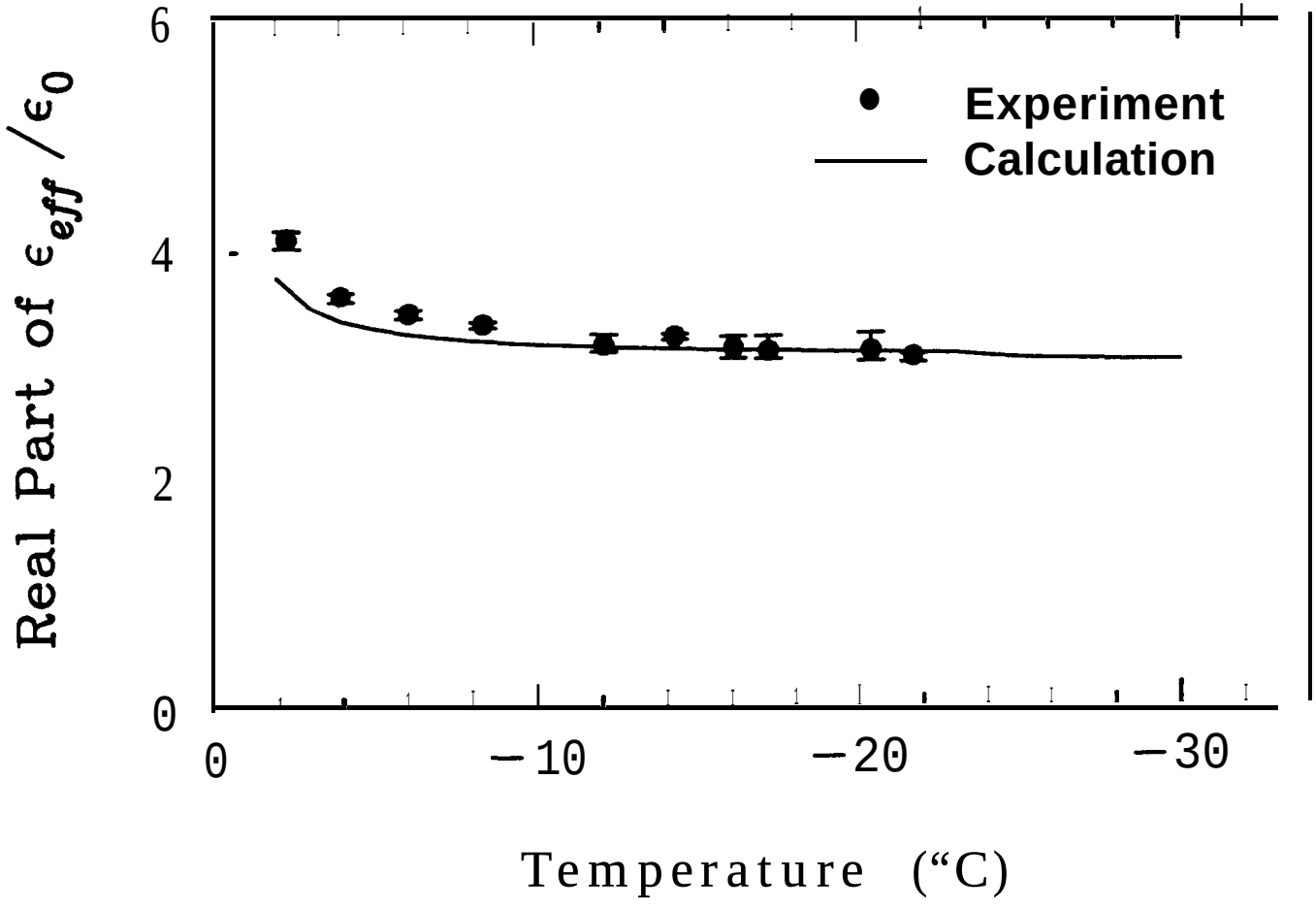

nahiem

FIG. 7a

(a) Shape Variations: Imaginary Part

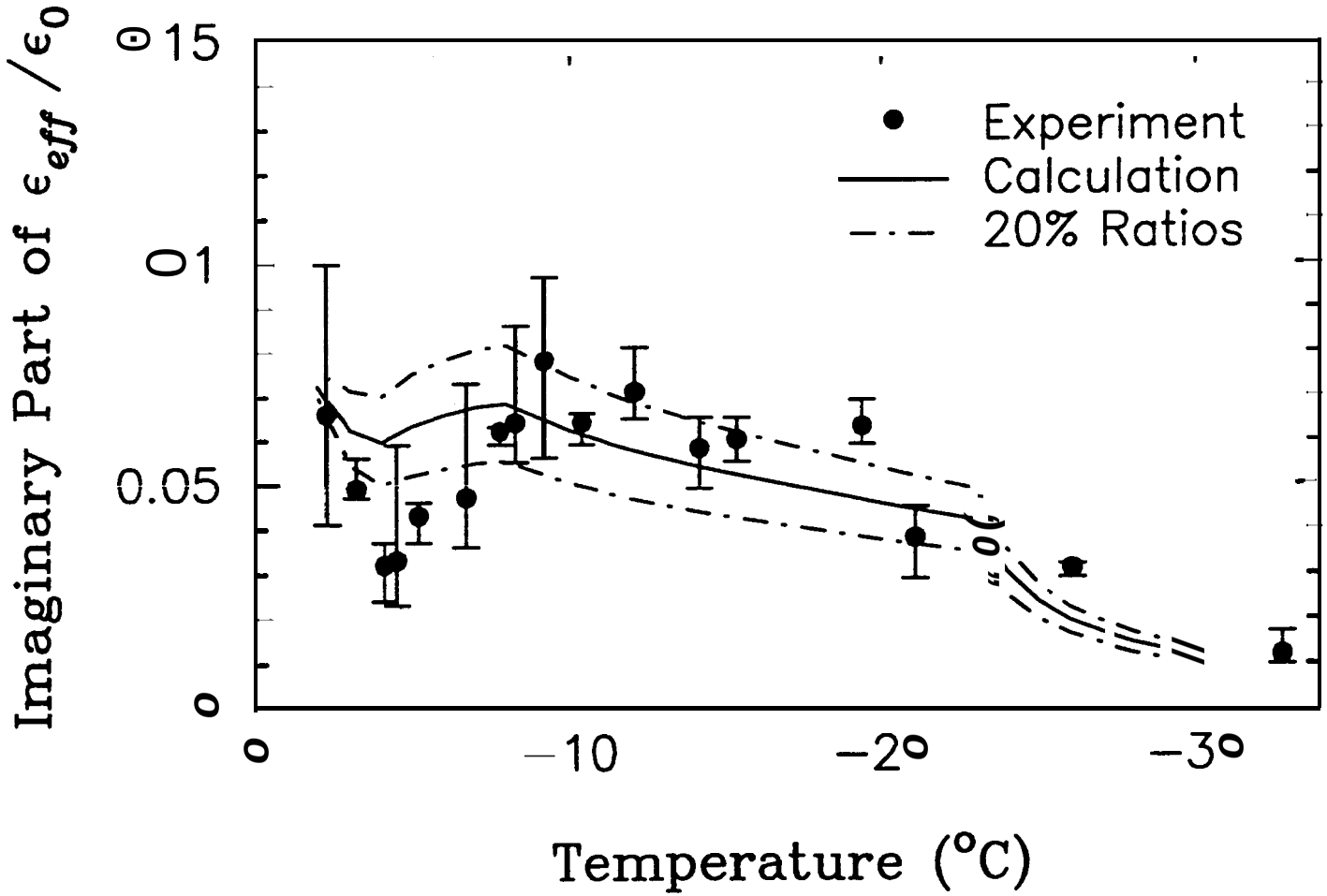

FIG. 7b

(b) Shape Variations: Real Part

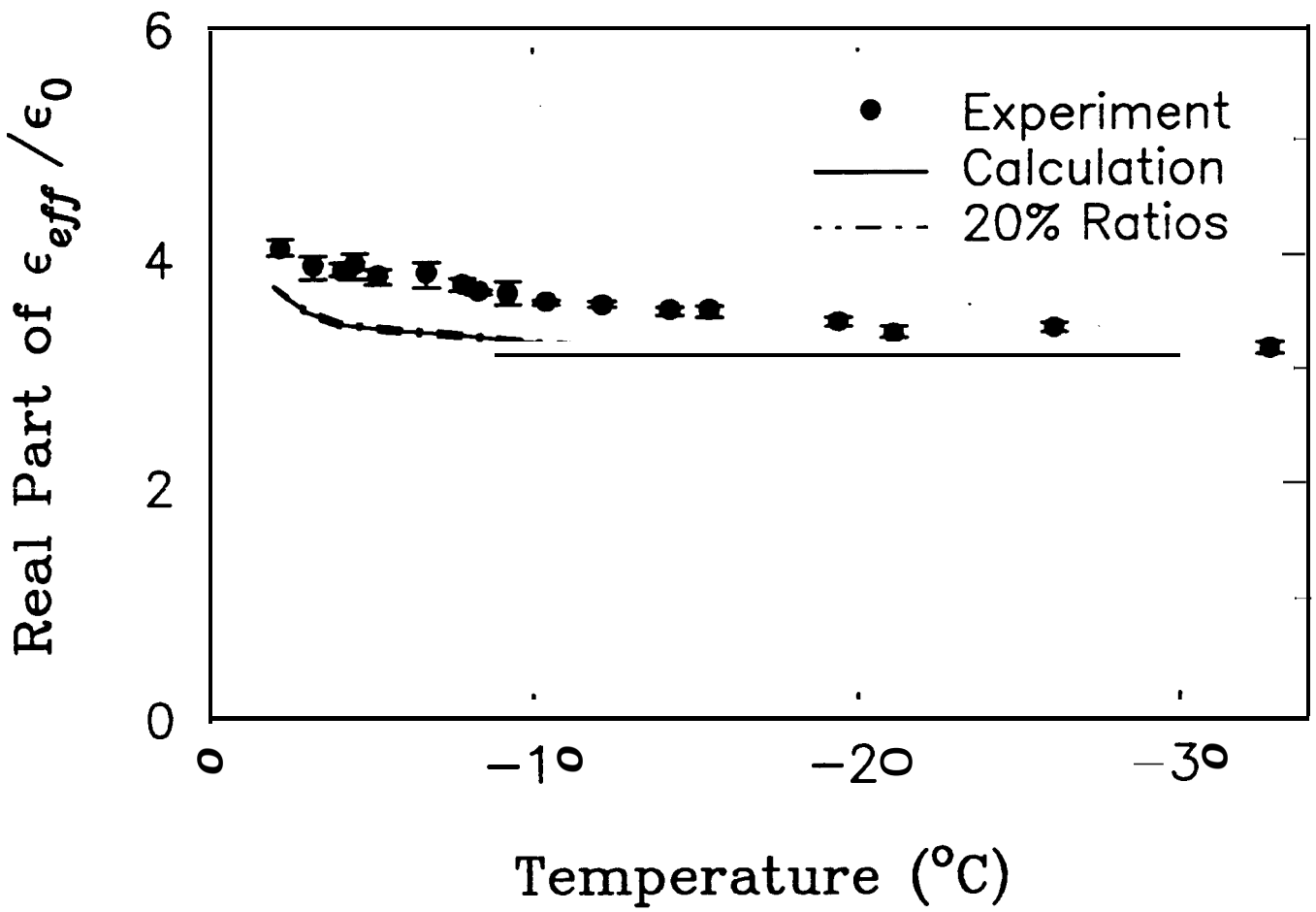

FIG, 8a

(a) Density Variations: Imaginary Part

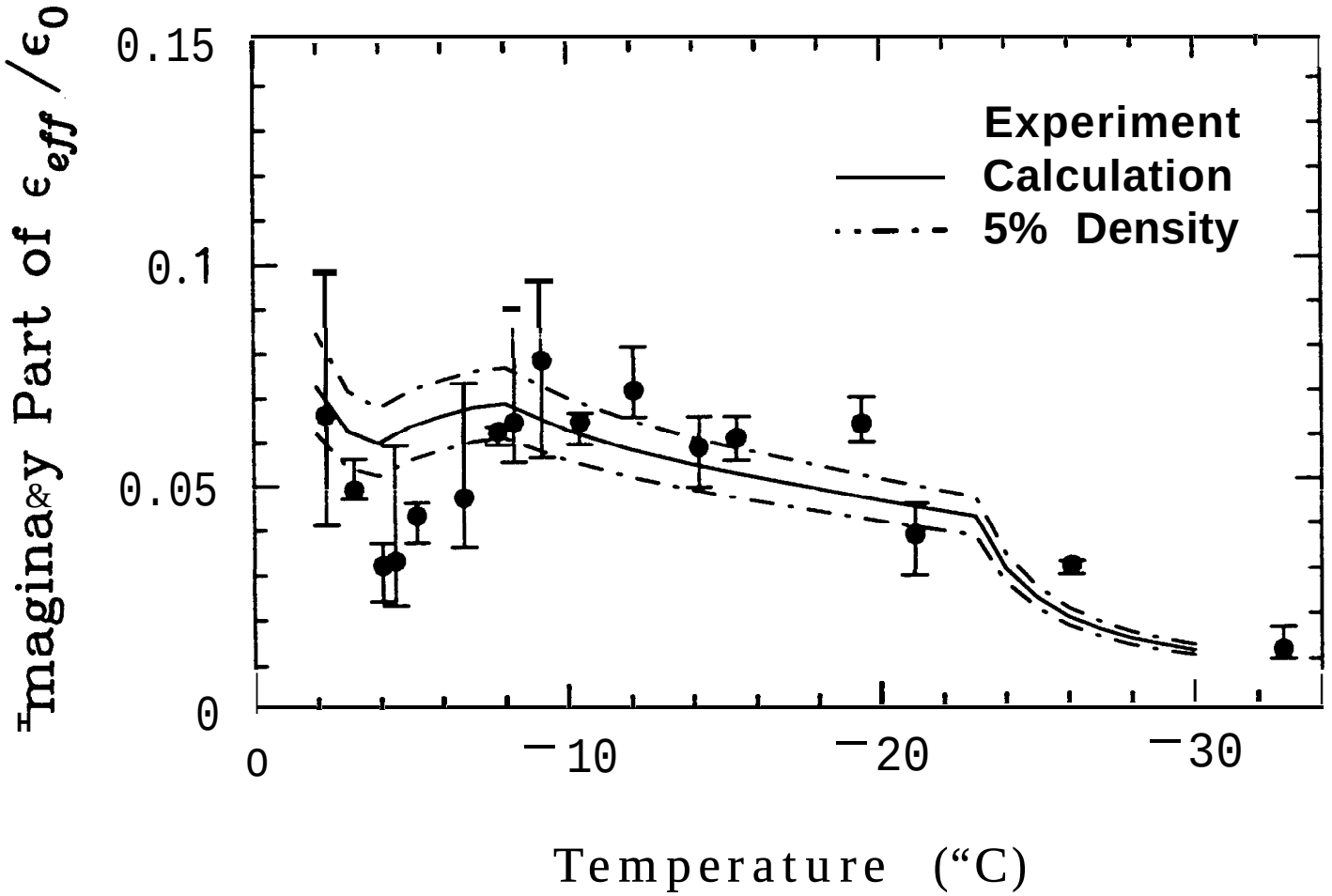

nahiem

FIG. 8b

(b) Density Variations: Real Part

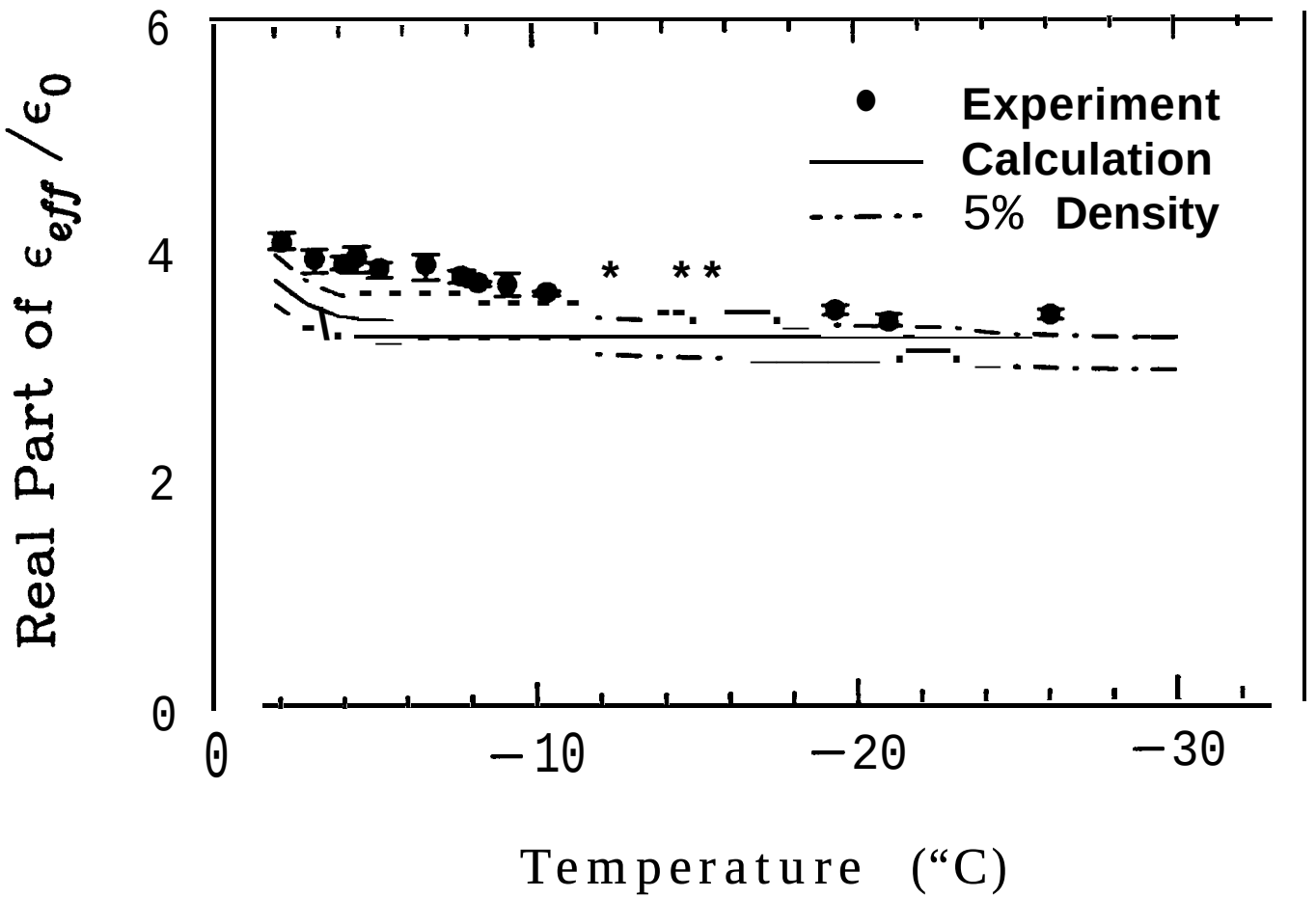

nahiem